KRONOS FUSION ENERGY

PAPER 2.12 · THE KRONOS 2026 SERIES

From Breakdown to Flat-Top: Solenoid-Free Startup and Disruption-Free Ramp Access for a Negative-Triangularity Spherical-Tokamak Breeder

A spherical tokamak (ST) has almost no inboard room for a central solenoid, so it cannot induce and ramp its plasma current the way a conventional tokamak does; startup is…

Read it live — 3-D model · physics validator · film series

BY P I FORD AND G L KULCINSKI

2026 · EDITORIAL EDITION

THE OFFICIAL RECORD

What this document is, and how to read its numbers

This is a combined editorial. It gathers, in one volume, the two design studies Kronos Fusion Energy released in 2026 — a compact spherical-tokamak tritium/helium-3 breeder and a deuterium–helium-3 tandem-mirror generator — together with the intellectual-property estate, the people, and, in the internal edition, the full commercial case. The scientific text is the same text that appears in the arXiv preprints and the journal submissions; the editorial adds the apparatus a reader needs to hold the whole program at once, and nothing in the physics is altered to fit it.

THE HONESTY STANCE IS THE ASSET

Every headline quantity carries an **evidence class** — DERIVED RECOMPUTED MEASURED REQUIREMENT — and, where a number is a modelled extrapolation rather than a demonstrated value, it is labelled as such and its downside is shown next to it. Several quantities in the underlying corpus moved after first publication; where a value has been withdrawn or restated, the record says so plainly. This is deliberate: a diligence team will find the load-bearing assumptions, so the document surfaces them first.

TWO EDITIONS

This volume is issued in two editions. The **public edition** (light) carries the physics and the design only — no dollar, price, or per-kilogram figure appears anywhere in it. The **internal edition** (dark) adds the economics, the funding architecture, and the defense-commercial analysis, and is marked *Confidential* accordingly; it is not for public distribution. Where the commercial case rests on a modelled assumption rather than a demonstrated one, it is labelled as such and its downside is shown alongside it, on the same terms as the physics.

TITLE	The Kronos Fleet — Hyperion · Aegis · MetroVolt: A Combined Design & Commercialization Study
AUTHOR	Priyanca Ford, Founder & CEO, on behalf of Kronos Fusion Energy
EDITION	2026 Combined Editorial · first issue
COMPANION WORKS	The five-paper arXiv drop — (1) Breeder, (2) Burner, (3) REBCO magnet & tape, (4) Direct Energy Conversion, (5) AI/ML/Quantum control — with matching numbered Zenodo deposits, plus the IOP journal and IAEA-FEC submissions. Patents were filed before the drop.
NAMING	Hyperion = the breeder; Aegis (defense) and MetroVolt (data-center) = one generator in two housings. Internal mode letters (D1, L) do not appear on public surfaces.
STATUS	Conceptual design & simulation study. Nothing herein is a construction commitment.

HOW TO READ THIS VOLUME

The fleet at a glance, and the way its numbers are marked

This volume opens with *Orientation*, presents the five research papers as a bound sequence, and closes with the *Apparatus*. *Foundations* sets out the three general results both machines rest on. *Paper One* is the Hyperion breeder; *Paper Two* the Aegis / MetroVolt generator; *Papers Three, Four and Five* are the enabling science — high-field REBCO magnets and tape, direct energy conversion, and the AI / ML / quantum control stack. A *Digital Twin & 3-D Model* part follows, then the *Environmental* profile. The *Economics* and levelized cost and the *Business Case* and diligence record appear in the internal edition only; the *Simulations* proof record and the Apparatus — patent portfolio, team, limitations, and sources — close both editions.

THE FLEET AT A GLANCE

	HYPERION	AEGIS	METROVOLT
Role	Strategic-isotope foundry	Defense installation power	Campus power
Machine	**Spherical tokamak**	**Tandem mirror**	**Tandem mirror**
Fuel	Deuterium–tritium	Deuterium–helium-3	Deuterium–helium-3
Delivers	Tritium · ^{3}He · 14 MeV n	Resilient installation power	Firm campus power
Physics bar	**Fusion gain only**	Closure (gates named)	Closure + lunar ^{3}He
In the fleet	Breeds the fuel	Proves the generator	Commercial destination

HOW THE NUMBERS ARE MARKED

Every headline quantity carries an evidence class — DERIVED from first principles, RECOMPUTED from raw data, MEASURED in hardware, or a REQUIREMENT yet to be met. Financial figures carry a case label and are confined to the internal (confidential) edition. Values that moved after first publication are shown as withdrawn or restated rather than quietly changed. A capability you can evaluate is one whose limits are on the page.

ABSTRACT

From Breakdown to Flat-Top: Solenoid-Free Startup and Disruption-Free Ramp Access for a Negative-Triangularity Spherical-Tokamak Breeder

A spherical tokamak (ST) has almost no inboard room for a central solenoid, so it cannot induce and ramp its plasma current the way a conventional tokamak does; startup is therefore a defining physics and engineering constraint rather than a solved preliminary. We formalise and quantify a solenoid-free startup and ramp path for the Kronos Hyperion breeder (design point plasma current $I_p = 9.66\,MA$, fusion gain $Q = 3.076$, $P_{\text{fus}} = 85.04\,MW$, negative triangularity $\delta = -0.30$, on-axis field $B_0 = 8\,T$, centrepost peak field $16.84\,T$, elongation $\kappa = 2.0$, major radius $R_0 = 1.20\,m$, aspect ratio $A = 2.5$). We write the poloidal-flux (current-diffusion) equation with an explicit non-inductive source, close the volt-second budget through a Poynting/Ejima accounting, and state the helicity-balance, electron-Bernstein-wave pre-ionization, and current-drive figure-of-merit relations as governing equations. The flux budget resolves the register anchor $\Psi_p \approx 20\,weber$ into a $14.5\,weber$ external-inductive, $5.8\,weber$ internal-inductive, and $5.8\,weber$ resistive (Ejima) partition, cross-checked against the empirical $2.0\,weber/MA$ Doublet-III rule ($19.3\,weber$). A reduced current-diffusion integrator whose non-inductive fixed point is $I_p^{\star} = I_{\text{CD}}/(1 - f_{\text{bs}}) = 8.16/0.845 = 9.66\,MA$ reaches 95% of flat-top in $42\,s$ at a disruption-benign ramp rate of $0.22\,MA/s$ and an inductive loop voltage below $1.4\,V$; the driven current $8.16\,MA$ (118.5 MW neutral-beam current drive, $\gamma_{\text{CD}} = 0.331$) and the bootstrap current $1.50\,MA$ close the $9.66\,MA$ balance exactly. The ramp corridor stays below the Greenwald limit at $f_G = 0.30$ and holds $q_{95} > 3$ throughout, and a runaway-electron avalanche band of 4.8–$8.2\,MA$ is met by a precursor stack whose lead times ($31\,ms$ physics-informed, $47.2\,ms$ fused-magnet) clear the $30\,ms$ shattered-pellet-injection requirement. Every number is a frozen anchor in the Kronos de-risking register. We flag one honest gate: the ramp is stated here as a quantified strategy with a bounded volt-second and current-drive budget, not as a closed-loop controlled sequence, and the bootstrap fraction carries a model-to-model spread that we report rather than average away.

Open-access deposit (code & data, CC BY 4.0): DOI 10.5281/zenodo.22645760 · Zenodo community *kronos_fusion_energy*. Explore it live: interactive 3-D model · physics validator.

Keywords: solenoid-free startup · non-inductive current ramp · helicity injection · electron Bernstein waves · bootstrap current · runaway electrons · spherical-tokamak breeder

CONTENTS

Table of Contents

NOMENCLATURE

Symbols, units, and the names of things

Q	plasma (fusion) gain, P_{fus}/P_{aux}
Q_E	engineering gain, net electric out / recirculating in
H_{98}	confinement enhancement over the IPB98(y,2) scaling
Z_{eff}	effective ion charge
c_{ee}	electron–electron bremsstrahlung leading coefficient, 2.120022 (exact)
τ_E	energy confinement time
I_p	plasma current
R_0, a	major radius, minor radius
κ, δ	elongation, triangularity
β_N	normalized plasma beta (Troyon-normalized)
TBR	tritium breeding ratio
DEC	direct energy conversion
CF	plant capacity factor (availability)
FOAK / NOAK / BOAK	first / n^{th} / best of a kind
Hyperion	the ST breeder (internal: Mode D2)
Aegis	the generator, defense/installation housing (internal: Mode M)
MetroVolt	the generator, data-center housing (Mode M)

§ 1

Introduction

THE SOLENOID-FREE IMPERATIVE

The central solenoid (CS) that a conventional tokamak uses to induce and ramp its plasma current occupies the bore of the machine, and its available flux swing scales with the cross-sectional area it can enclose on the inboard side. A spherical tokamak trades exactly that inboard volume for a slender, high-field centrepost: the low aspect ratio $A = R_0/a$ that gives the ST its high natural elongation, high bootstrap fraction and compact neutron-source geometry [1,2,3] also removes the room a CS would need. In the Hyperion breeder the inboard leg is a demountable REBCO centrepost carrying peak field $16.84\,T$; there is no transformer core. Solenoid-free startup is therefore not an operational convenience but a first-order design constraint. The question this paper answers is quantitative: with no inductive transformer, what flux, what power, and what trajectory take the machine from cold gas to a $9.66\,MA$ non-inductive flat-top, and does that trajectory stay clear of the density, current-profile and runaway limits that make a ramp dangerous?

THE KRONOS HYPERION OPERATING POINT

Hyperion is a compact, negative-triangularity ST breeder. Its frozen design point — re-anchored and audited in the de-risking register [35] — is $I_p = 9.66\,MA$, $Q = 3.076$, $P_{\rm fus} = 85.04\,MW$, normalised beta $\beta_N = 1.53$, energy-confinement time $\tau_E = 0.358\,s$ at $H_{98} = 1.0$ (stored energy $W = 16.06\,MJ$), edge safety factor $q_{95} = 3.0$, $R_0 = 1.20\,m$, $a = 0.48\,m$, $A = 2.5$, $\kappa = 2.0$, $\delta = -0.30$, and on-axis field $B_0 = 8\,T$. Negative triangularity is chosen because it accesses good core confinement without the H-mode pressure pedestal and its edge-localised-mode cycle [4,5]; the resulting quiet, ELM-free L-mode edge is an operational asset that also removes a class of transient edge loads from the ramp. The centrepost field $16.84\,T$ is the breeder magnet; the $26.49\,T$ plug coil that appears elsewhere in the Kronos programme belongs to the separate D–^{3}He tandem-mirror burner and plays no role here. We keep the two magnets distinct throughout.

PRIOR ART

Solenoid-free startup has an experimental record on the world's STs and on conventional tokamaks operated at low loop voltage. The techniques divide into three families [6]. *Pre-ionization and low-voltage assist*: electron-cyclotron heating lowers the required breakdown electric field — Lloyd *et al.*\ demonstrated ECH-assisted startup on DIII-D at $E \simeq 0.15\,V/m$, roughly half the Ohmic value [7] — and on an overdense ST edge the electron Bernstein wave (EBW) is the accessible branch for both pre-ionization and non-inductive drive [8,9]. *Helicity injection*: coaxial helicity injection (CHI) builds closed flux surfaces without a transformer, demonstrated on HIT-II and NSTX, where transient CHI reached $1\,MA$ from only $258\,mweber$ of solenoid flux — a $\sim 50\%$ flux saving — at an efficiency near $10\,A/J$ [10]. *Non-inductive drive and bootstrap*: neutral-beam, electron-cyclotron and lower-hybrid current drive grow and then sustain the current, with the self-generated bootstrap current supplying the aligned balance of a steady state [11,12,13]. The physics of each ingredient is mature; what a compact nuclear ST needs is a single, quantified budget that shows the ingredients *combine* to reach a specific operating current along a specific, limit-avoiding trajectory. That budget is the contribution here.

CONTRIBUTION

This paper (i) states the governing equations of a solenoid-free start — the poloidal-flux diffusion equation with a non-inductive source, the Poynting/Ejima volt-second balance, the helicity-injection balance, the EBW breakdown power balance, and the current-drive figure of merit (§3); (ii) closes the flux and current budget of the Hyperion ramp against the frozen anchors, resolving the $20\,weber$ register number into its inductive and resistive parts and reconciling the $118.5\,MW$ current-drive power with the $8.16\,MA$ driven current and $1.50\,MA$ bootstrap current (§5); (iii) gives the numerical formulation and the NVIDIA GPU HPC campaign that produced the results, with a temporal-convergence verification (§4); (iv) demonstrates a disruption-free ramp corridor below the Greenwald limit and above the $q = 2$ surface, with a runaway-electron avalanche budget met by a precursor stack (§5); and (v) benchmarks each number against the published ST and tokamak-startup literature (§6). We cite the companion papers of the Kronos 2026 series where they carry the load: the steady-state current-drive paper [27] for the flat-top that the ramp hands off to, the equilibrium and ideal-MHD paper [28] and the vertical-stability paper [29] for the shape the PF set must hold, the poloidal-field-coil paper [30] for the coil currents that provide the outboard flux swing, the disruption and runaway paper [31] for the mitigation case, and the real-time control-suite paper [32] for the ramp controller that closes the loop.

§ 2

The startup problem: formal statement

WHY THE TRANSFORMER IS UNAVAILABLE

A CS drives the plasma by mutual induction: a changing solenoid current $I_{\mathrm{CS}}(t)$ links a flux $\Psi_{\mathrm{CS}} = M_{\mathrm{CS,p}} I_{\mathrm{CS}}$ to the plasma, and the loop voltage $V_\ell = -\dot{\Psi}_{\mathrm{CS}}$ both breaks down the gas and drives I_p. The deliverable flux swing is bounded by $\Delta\Psi_{\mathrm{CS}} \lesssim \pi a_{\mathrm{CS}}^2\,\Delta B_{\mathrm{CS}}$, set by the solenoid bore a_{CS} and its peak field. In an ST the inboard bore is consumed by the centrepost, so $a_{\mathrm{CS}} \to 0$ and $\Delta\Psi_{\mathrm{CS}} \to 0$: the transformer term vanishes and the plasma must be initiated and grown by the flux and current the *outboard* coils, the injected helicity, and the non-inductive drive can supply. The formal problem is to find a trajectory $\{I_p(t), n_e(t), T_e(t), \psi(\rho, t)\}$ from breakdown to flat-top that (a) satisfies the poloidal-flux balance at every instant, (b) never violates the density, current-profile or runaway limits, and (c) terminates at the non-inductive fixed point $I_p = 9.66\,MA$ where drive plus bootstrap balance resistive decay. Figure 1 sketches the four-phase strategy the equations below make concrete.

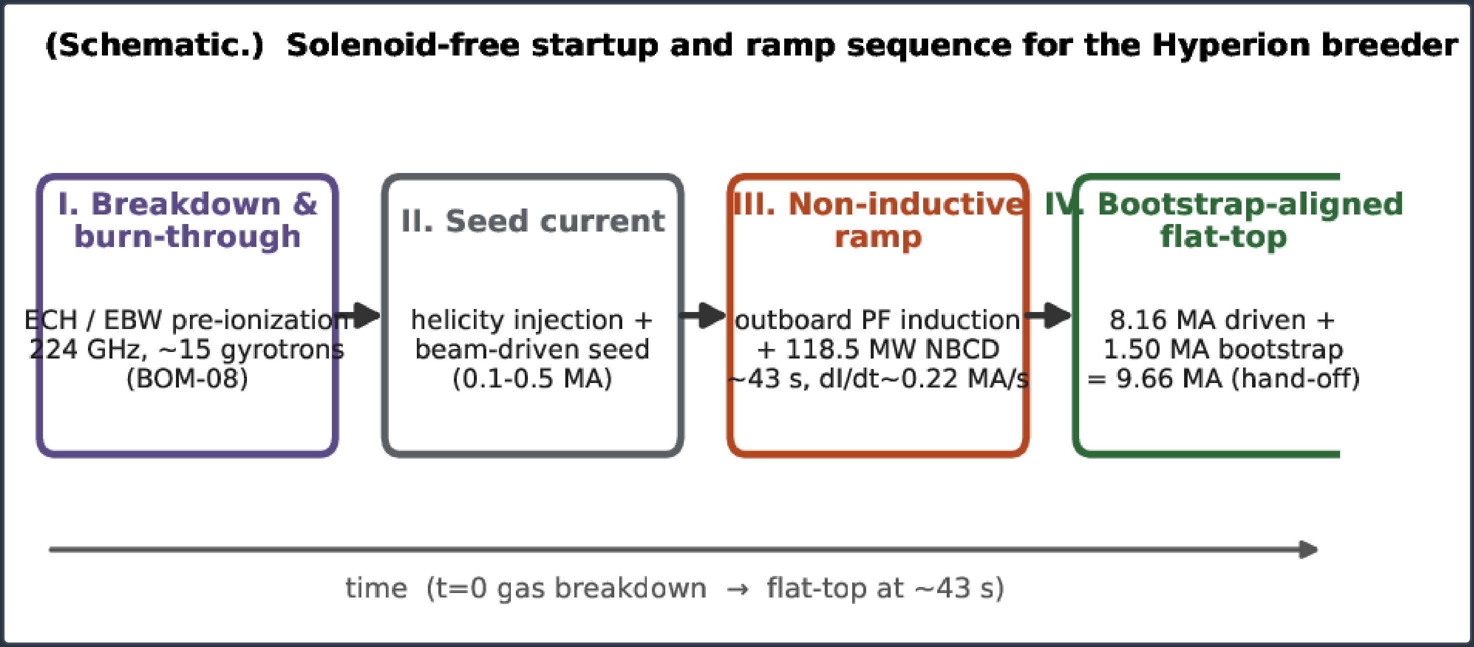

(Schematic.) The four-phase solenoid-free path: (I) EBW/ECH pre-ionization and burn-through; (II) a helicity- and beam-driven seed current; (III) an outboard-PF-plus-neutral-beam non-inductive ramp; (IV) hand-off to the bootstrap-aligned $9.66\,MA$ flat-top of the current-drive companion [27]. Current and time annotations trace to the register serials BR-CX-07, BOM-07 and BOM-08 [35].

VOLT-SECOND ACCOUNTING

The flux the machine must build to hold the flat-top current has an inductive part, stored in the poloidal field, and a resistive part, dissipated while the current is established. Following the Poynting-theorem accounting of Ejima *et al.* [14], the surface flux consumed to reach the current flat-top is

$$\Psi_{\mathrm{tot}} = \underbrace{L_p I_p}_{\text{inductive}} + \underbrace{C_E\,\mu_0 R_0 I_p}_{\text{resistive}}, \qquad L_p = \mu_0 R_0 \left[\ln\frac{8R_0}{a} - 2 + \frac{\ell_i}{2}\right],$$

with internal inductance ℓ_i and the empirical Ejima coefficient $C_E \simeq 0.4$. Equation (1) is the budget a purely inductive machine would have to supply from its transformer. A solenoid-free machine cannot supply the inductive term from a CS and does not want to pay the resistive term inductively at all; the strategy is to build $L_p I_p$ from the poloidal flux *linked to the driven current itself* plus a limited outboard-coil swing, and to carry the resistive term with continuous non-inductive drive. Section 5 evaluates equation (1) at the Hyperion point and shows the partition (figure 2).

§ 3

Governing equations

THE POLOIDAL-FLUX (CURRENT-DIFFUSION) EQUATION

Let $\psi(R, Z, t)$ be the poloidal flux per radian. Amp\`ere's law in axisymmetry gives the toroidal current density from the Grad–Shafranov (elliptic) operator,

$$\mu_0 R j_\phi = -\Delta^* \psi, \qquad \Delta^*\psi \equiv R^2 \nabla\cdot\left(\frac{\nabla\psi}{R^2}\right) = R\frac{\partial}{\partial R}\left(\frac{1}{R}\frac{\partial\psi}{\partial R}\right) + \frac{\partial^2\psi}{\partial Z^2}.$$

The mean-field parallel Ohm's law relates the inductive electric field to the difference between the total and the non-inductive (bootstrap + current-drive) current,

$$E_\parallel = \eta_\parallel\big(j_\parallel - j_{\rm bs} - j_{\rm cd}\big), \qquad E_\parallel = -\frac{1}{R}\frac{\partial\psi}{\partial t},$$

where $\eta_\parallel$ is the neoclassical parallel resistivity (Spitzer–H\"arm [15] corrected by the trapped-particle factor of Sauter [12]). Combining (2)–(3) yields the current-diffusion equation for the poloidal flux,

$$\boxed{\frac{\partial\psi}{\partial t} = \frac{\eta_\parallel}{\mu_0}\Delta^*\psi + \eta_\parallel R\left(j_{\rm bs} + j_{\rm cd}\right)}$$

— a nonlinear parabolic equation in which the first term diffuses poloidal flux resistively and the second is the non-inductive source that, at steady state ($\partial_t\psi = 0$), pins the current profile so that $-\Delta^*\psi/\mu_0 R = j_{\rm bs} + j_{\rm cd}$. For a numerical solution it is convenient to reduce (4) to one dimension on a flux-surface label ρ (the square-root of normalised toroidal flux). Writing $\psi(\rho, t)$ and flux-surface-averaging, the standard transport form is

$$\sigma_\parallel\frac{\partial\psi}{\partial t} = \frac{1}{\mu_0\rho}\frac{\partial}{\partial\rho}\left[\rho\, G(\rho)\,\frac{\partial\psi}{\partial\rho}\right] + \langle j_{\rm ni}\cdot B\rangle/\langle B\rangle,$$

with $\sigma_\parallel = 1/\eta_\parallel$ the parallel conductivity, $G(\rho)$ the geometric metric coefficient $\langle|\nabla\rho|^2/R^2\rangle$, and $j_{\rm ni} = j_{\rm bs} + j_{\rm cd}$. Equation (5) is the RAPTOR- and TSC-class flux-diffusion equation [16,17]; its natural boundary conditions are the on-axis regularity $\partial_\rho\psi|_0 = 0$ and an edge condition set by the enclosed current, $\partial_\rho\psi|_a \propto I_p(t)$, which the outboard poloidal-field coils and the driven current together supply [30]. The characteristic timescale of (5) is the resistive (skin) time

$$\tau_R = \frac{\mu_0 a^2}{\eta_\parallel},$$

which at a ramp-phase electron temperature of a few keV is $\mathcal{O}(15\,s)$ and rises steeply ($\eta_\parallel \propto T_e^{-3/2}$) as the plasma heats, so the current relaxes over a few tens of seconds — the physical origin of the slow, disruption-benign ramp quantified below.

HELICITY INJECTION AND TAYLOR RELAXATION

Before the driven current dominates, a seed current can be established by helicity injection. Magnetic helicity $K = \int_V \quad A\cdot \quad B\,dV$ obeys the balance [10,6]

$$\frac{dK}{dt} = 2\,V_{\rm inj}\,\Psi_{\rm inj} - \frac{2}{\tau_K}K,$$

where $V_{\rm inj}$ is the injector voltage, $\Psi_{\rm inj}$ the injected poloidal flux threading the injector electrodes, and τ_K the helicity dissipation time. Sustained injection drives toroidal current when the drive term exceeds resistive decay. Under Taylor relaxation to a minimum-energy (constant-λ) state the amplified toroidal current relates to the injected current by the current-amplification factor

$$\frac{I_\phi}{I_{\rm inj}} \simeq \frac{\lambda\,\Psi_{\rm inj}}{\mu_0 I_{\rm inj}} \gg 1,$$

the mechanism by which transient CHI produced $1\,MA$-class currents from sub-Wb injector flux on NSTX [10]. For Hyperion the helicity seed is booked as one route to the 0.1–$0.5\,MA$ seed current of phase II (figure 1); the beam-driven alternative is discussed in §3.4.

BREAKDOWN AND BURN-THROUGH: THE EBW/ECH POWER BALANCE

Because there is no large loop voltage to drive Townsend avalanche, breakdown is electron-cyclotron assisted. The zero-dimensional electron power balance through burn-through is

$$\frac{d}{dt}\left(\tfrac{3}{2}n_eT_e\right) = P_{\rm ECH} - P_{\rm rad} - P_{\rm ion} - P_{\rm conv},$$

with $P_{\rm ECH}$ the absorbed electron-cyclotron power, $P_{\rm rad}$ the line- and bremsstrahlung-radiated power, $P_{\rm ion} = n_e n_0 \langle\sigma v\rangle_{\rm ion}\varepsilon_{\rm ion}$ the ionization sink, and $P_{\rm conv}$ the convective/conductive loss along open field lines. Wave access sets which branch delivers $P_{\rm ECH}$. At $B_0 = 8\,T$ the fundamental electron-cyclotron frequency is $f_{ce} = eB/2\pi m_e = 224\,\text{Hertz}$; $theratioofplasmatocyclotronfrequencyattheintendedstartupdensityis$\omega_pe/\omega_ce\simeq0.80 $inthecore(underdense, sotheordinaryO - modeisabsorbed), buttheedgeisoverdense($\omega_pe/\omega_ce>1 $), wheretheO - modeiscutoffandtheelectronBernsteinwave --- reachedbyO--X--Bmodeconversion --- istheaccessiblebranch \quad laqua2007. TheHyperionpre - ionizationsystemissizedat$ \!15$gyrotronsat$1 MW$near$224 [redacted] (register serial BOM-08 [35]). Equation (9) and the access condition are evaluated in §5.5 and figure 5.

NON-INDUCTIVE CURRENT DRIVE AND THE DRIVEN/BOOTSTRAP SPLIT

Away from breakdown, the current is grown and sustained non-inductively. The efficiency of external current drive is captured by the dimensionless figure of merit [11,13]

$$\gamma_{\rm CD} = \frac{\bar{n}_e\,R_0\,I_{\rm CD}}{P_{\rm CD}} \quad \left[10^{20}\,\mathrm{A\,W^{-1}\,m^{-2}}\right],$$

so that the driven current is $I_{\rm CD} = \gamma_{\rm CD}P_{\rm CD}/(\bar{n}_eR_0)$. Neutral-beam current drive is the primary actuator (register BOM-07): $118.5\,MW$ of $1\,MeV$ negative-ion deuterium beams across eight beamlines drives $I_{\rm CD} = 8.16\,MA$ at $\gamma_{\rm CD} = 0.331$ — inside the 0.20–0.40 band expected for an ST at this temperature — against a line-averaged density $\bar{n}_e = f_G n_{\rm GW} = 0.30 \times 13.34e19\,/cubicm = 4.0e20\,/cubicm$. The remainder of the current is self-generated. The bootstrap current fraction from the Sauter formulation at the frozen operating point (register BR-L2-A6) is

$$f_{\rm bs} = \frac{I_{\rm bs}}{I_p} = 0.155, \qquad I_{\rm bs} = f_{\rm bs}I_p = 1.50\,\mathrm{MA},$$

so that $I_{\rm CD} + I_{\rm bs} = 8.16 + 1.50 = 9.66\,MA = I_p$: the non-inductive balance closes exactly at the flat-top. The bootstrap fraction is deliberately low — the machine is current-drive-dominated, not bootstrap- dominated — which simplifies the ramp because the profile need not be sculpted to a high-bootstrap alignment, but which also means the resistive term in equation (1) must be carried continuously by the beams.

THE DISRUPTION-FREE RAMP: THE THREE LIMIT CONSTRAINTS

A ramp is dangerous where it crosses a stability boundary. The trajectory $\{I_p(t), \bar{n}_e(t)\}$ is constrained by three inequalities that must hold at every instant.

Density. The line-averaged density must stay below the Greenwald limit,

$$\bar{n}_e(t) \;<\; n_{\rm GW}(t) = \frac{I_p(t)}{\pi a^2} \quad \left[10^{20}\,\mathrm{m^{-3}},\ I_p\ \mathrm{in\ MA}\right],$$

which at fixed Greenwald fraction f_G traces a straight corridor in the $(I_p, \bar{n}_e)$ plane (figure 2); operating at $f_G = 0.30$ leaves a $3.3\times$ margin.

Current profile. The edge safety factor must stay above the $q = 2$ external-kink boundary. Since $q_{95} \propto B_0a^2\kappa_{\rm eff}/(R_0I_p)$ at fixed shape, ramping I_p from the seed toward $9.66\,MA$ lowers q_{95} monotonically toward its flat-top value 3.0, remaining above $q = 2$ throughout; the internal q-profile, hollow while the seed and beam drive are off-axis, relaxes to a monotonic flat-top profile with $q_0 \gtrsim 1$ that avoids a low-order rational on axis (figure 4).

Runaways. During low-density breakdown and the early ramp, a runaway-electron seed can be produced by the Dreicer mechanism and amplified by close-collision avalanche [22,23]. The avalanche grows the runaway current as $dI_{\rm RE}/dt \simeq I_{\rm RE}/\tau_{\rm av}$ with $\tau_{\rm av} \propto (E/E_c - 1)^{-1}$, and in a reactor-scale current channel can reach a multi-MA plateau. The register bounds the Hyperion plateau band at 4.8–$8.2\,MA$ (BR-SX-10); §5.6 shows how the precursor stack meets it.

§ 4

Computational methodology: the NVIDIA GPU HPC campaign

DISCRETIZATION OF THE FLUX-DIFFUSION EQUATION

Equation (5) is discretized by a conservative finite-volume scheme on a uniform ρ-grid of N_ρ cells. The diffusion operator is written in flux form, $\partial_\rho[\rho G\, \partial_\rho \psi] \to (F_{j+1/2} - F_{j-1/2})/\Delta\rho$ with face fluxes $F_{j+1/2} = \rho_{j+1/2} G_{j+1/2}(\psi_{j+1} - \psi_j)/\Delta\rho$, giving a tridiagonal system. Time advance uses an implicit (θ-weighted Crank–Nicolson, $\theta = \frac{1}{2}$) step to remove the diffusive stability limit $\Delta t < \mu_0 \Delta\rho^2/2\eta_\parallel$; the nonlinear coupling of $\eta_\parallel(T_e)$ and the non-inductive source is resolved by Picard iteration to a relative tolerance 10^{-6} each step. The enclosed plasma current is recovered by quadrature,

$$I_p(t) = \frac{2\pi}{\mu_0}\left[\rho G\, \partial_\rho \psi\right]_{\rho=1},$$

and the surface loop voltage by $V_\ell(t) = 2\pi\, \partial_t \psi|_{\rho=1}$.

REDUCED CURRENT-BUILD MODEL

For the ramp-trajectory study we use a lumped reduction of (5) in which the current relaxes toward its non-inductively supported value on the skin time,

$$\frac{dI_p}{dt} = \frac{I_{\rm CD}(t) - (1 - f_{\rm bs}) I_p}{\tau_{\rm skin}}, \qquad I_{\rm CD} = \min\left[\frac{\gamma_{\rm CD} P_{\rm CD}(t)}{\bar{n}_e(I_p)\, R_0},\, I_{\rm driven}\right],$$

with $\bar{n}_e(I_p) = f_G I_p/\pi a^2$ (density follows current at fixed f_G) and the installed-NBCD ceiling $I_{\rm driven} = 8.16\, MA$. The fixed point of (14) is $I_p^\star = I_{\rm driven}/(1 - f_{\rm bs}) = 8.16/0.845 = 9.66\, MA$, so the reduced model reaches the frozen flat-top by construction; its content is the *trajectory* and the ramp time, not the endpoint.

FREE-BOUNDARY EQUILIBRIUM COUPLING AND THE CODE SUITE

The current-diffusion solve is coupled at each macro-step to a free-boundary Grad–Shafranov equilibrium so that the metric $G(\rho)$, the geometry of the negative-triangularity boundary, and the outboard-coil flux linkage are self-consistent along the ramp. The Kronos startup campaign runs the following codes, each named for the role it plays in this paper:

FreeGS / FreeGSNKE [18] — free-boundary equilibrium sequence along the ramp trajectory; supplies $G(\rho)$, the $\delta = -0.30$, $\kappa = 2.0$ boundary, and the PF-coil currents that set the edge condition of (5) (companion PF study [30]).
Poloidal-flux transport solver (in-house, RAPTOR/TSC-class [16,17]) — the discretization of §4.1 that integrates (5).
NEO and the **Sauter** model [12] — neoclassical conductivity and the bootstrap current of equation (11) (register BR-L2-A6).
TGLF/TGYRO [19] — turbulent-transport profile prediction feeding $T_e(\rho, t)$ and hence $\eta_\parallel$ along the ramp.
ASCOT5 [20] — Monte-Carlo orbit-following for the neutral-beam deposition and the driven-current profile $j_{\rm cd}(\rho)$.
DREAM [21] — coupled fluid–kinetic runaway-electron avalanche during breakdown and the early ramp, providing the plateau band of §5.6.
CGYRO [24] — the nonlinear-gyrokinetic quiescence at the operating point that the ramp delivers the plasma into (turbulence companion [34]).
Graph-neural-network and physics-informed precursor networks — disruption/ramp-to-limit warning (register BR-CX-31), §5.6. itemize

GPU ACCELERATION, PROBLEM SCALE, AND REPRODUCIBILITY

The campaign executed on the NVIDIA GPU HPC fleet (A100/H100/A10 class). The GPU-accelerated workloads are the free-boundary equilibrium sequences (hundreds of equilibria along each candidate ramp), the ASCOT5 orbit-following (order 10^6 markers per beam-deposition evaluation), the DREAM avalanche scans across the electric-field and density trajectory, and the training of the precursor networks; the reduced current-build integrator of (14) and the tridiagonal flux solve run at interactive speed and are used for the thousands-of-samples ramp-trajectory sweeps. All headline numbers are frozen anchors in the de-risking register [35] and every figure in this paper is regenerated by a single deposited script from those anchors. As a numerical-verification example, figure 7 shows the temporal convergence of the current-build integrator: the error in the flat-top current falls first-order in the time step Δt, confirming the integrator is converged at the step used for the trajectory figures.

§ 5

Results

THE FLUX BUDGET

Evaluating the volt-second balance (1) at the Hyperion point with $\ell_i = 0.8$ and $C_E = 0.40$ gives the partition of figure 2: an external-inductive flux $\Psi_{\text{ext}} = 14.5\,weber$, an internal- inductive flux $\Psi_{\text{int}} = 5.8\,weber$, an inductive total $\Psi_{\text{ind}} = 20.3\,weber$ that matches the register anchor $\Psi_p \approx 20\,weber$ (BR-CX-07), and a resistive (Ejima) flux $\Psi_{\text{res}} = 5.8\,weber$. The inductive total agrees with the empirical Doublet-III rule of $2.0\,weber/MA$ [14], which predicts $2.0 \times 9.66 = 19.3\,weber$ — an independent cross-check of the register number to within 5%. The design consequence is that the solenoid-free start must build $\sim 20\,weber$ of inductive poloidal flux without a transformer: a few Wb come from the limited outboard-PF swing [30], and the balance is carried by the flux linked to the driven current as it grows, with the $\sim 6\,weber$ resistive term supplied continuously by the beams rather than by a transformer flux swing.

QUANTITY	SYMBOL	VALUE	BASIS / SERIAL
external inductive flux	Ψ_{ext}	14.5 weber	eq. (1), $\ell_i = 0.8$
internal inductive flux	Ψ_{int}	5.8 weber	eq. (1)
inductive total	Ψ_{ind}	20.3 weber	matches $\Psi_p \approx 20$ (BR-CX-07)
resistive (Ejima) flux	Ψ_{res}	5.8 weber	$C_E \mu_0 R_0 I_p$, $C_E = 0.4$
Ejima empirical cross-check	—	19.3 weber	$2.0\,\text{Wb/MA} \times 9.66$
driven current (NBCD)	I_{CD}	8.16 MA	118.5 MW, γ_{CD}=0.331 (BOM-07)
bootstrap current	I_{bs}	1.50 MA	$f_{\text{bs}} = 0.155$ (BR-L2-A6)
flat-top current	I_p	9.66 MA	$I_{\text{CD}} + I_{\text{bs}}$ (BR-L1-A7)
ramp time to 95%	τ_{ramp}	42 s	eq. (14); ~43 s (BR-CX-07)

Solenoid-free flux and current budget at the Hyperion flat-top. Anchors from the de-risking register [35]; the Ejima cross-check from [14].

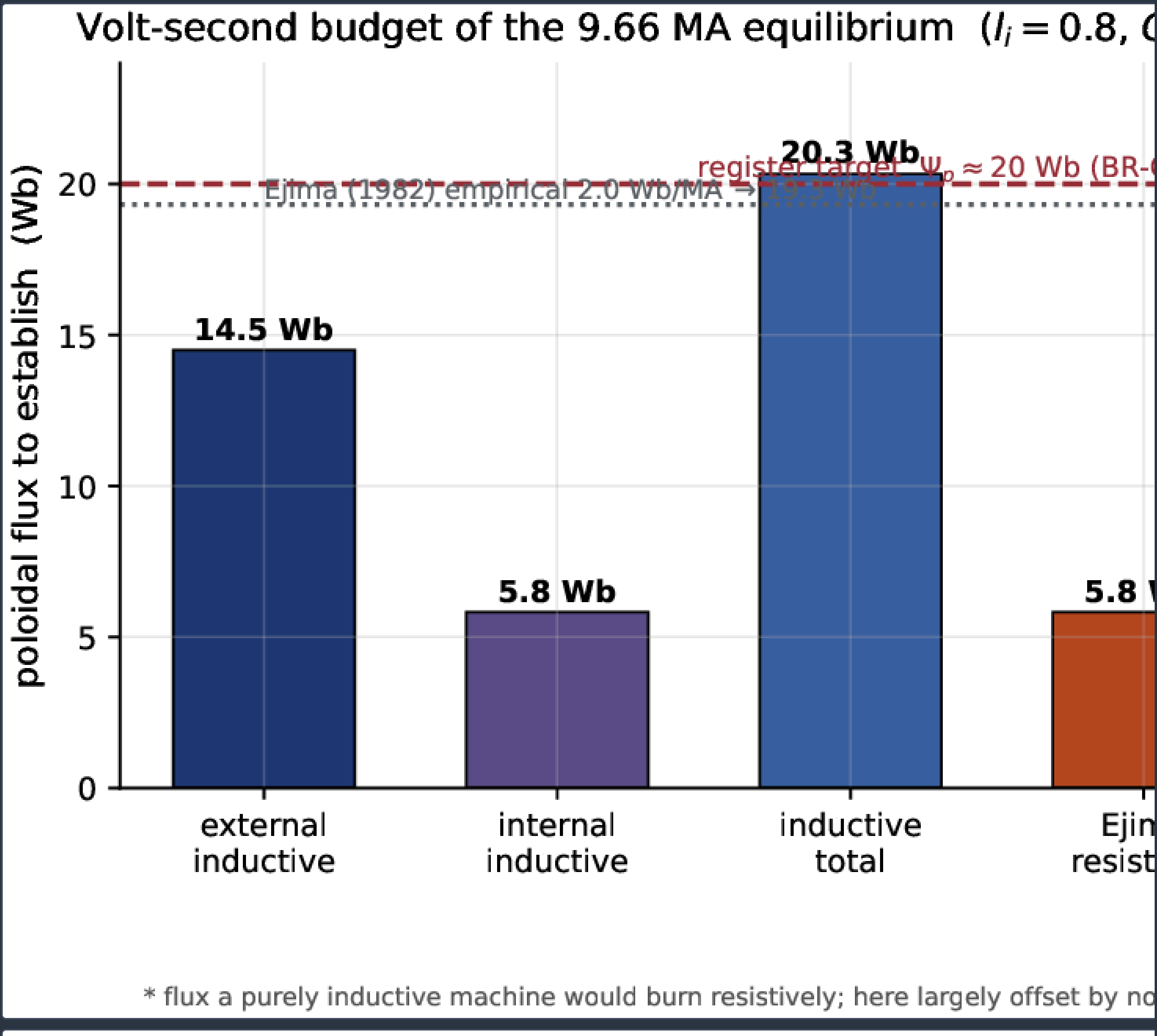
Volt-second budget of the 9.66 MA equilibrium (l_i = 0.8, C
poloidal flux to establish (Wb)
20
15
10
5
0
register target Ψp ≈ 20 Wb (BR-
Ejima (1982) empirical 2.0 Wb/MA → 19.3 Wb
14.5 Wb
5.8 Wb
20.3 Wb
5.8 W
external inductive
internal inductive
inductive total
Ejin resist
* flux a purely inductive machine would burn resistively; here largely offset by no

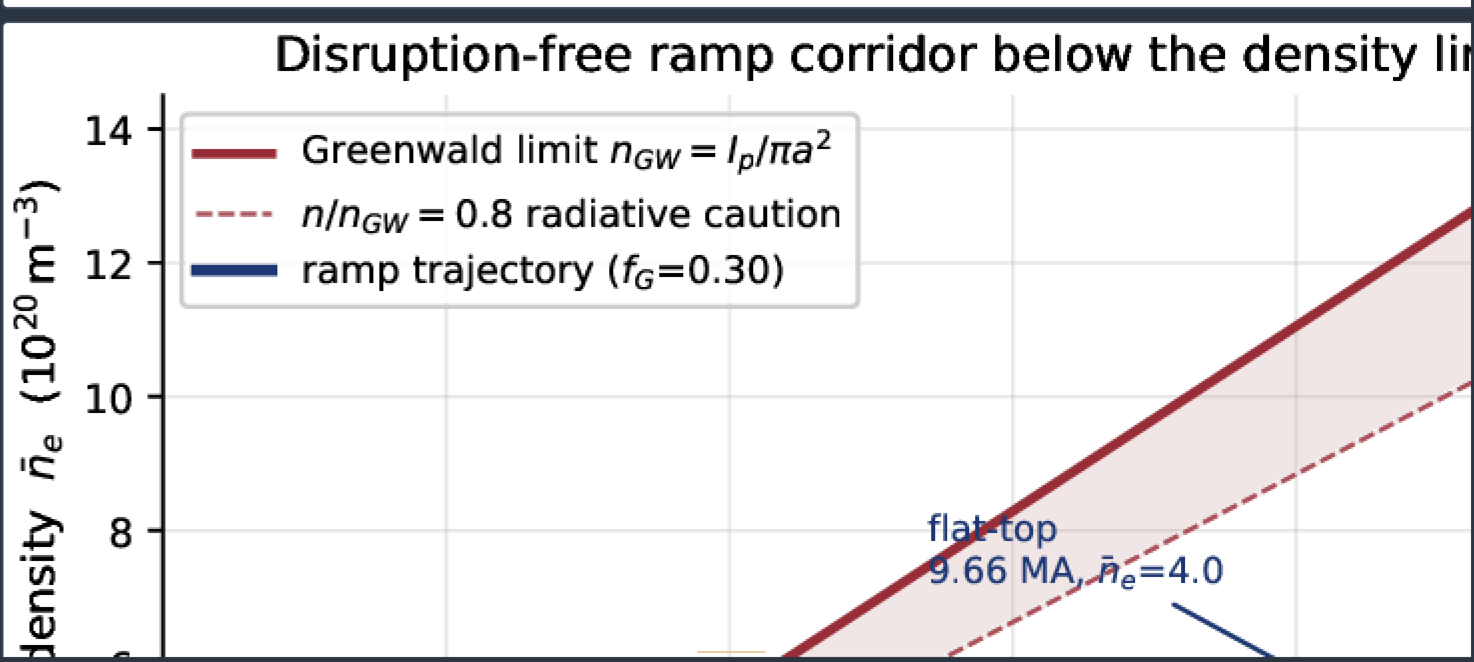
Disruption-free ramp corridor below the density li
density n̄e (10^20 m^-3)
14
12
10
8
Greenwald limit nGW = Ip/πa²
n/nGW = 0.8 radiative caution
ramp trajectory (fG=0.30)
flat-top
9.66 MA, n̄e=4.0

THE RAMP TRAJECTORY AND CURRENT BUILD

Integrating the reduced current-diffusion model (14) with $\tau_{\text{skin}} = 12\,s$ and a beam-power ramp over the first $8\,s$ produces the current build of figure 3: I_p reaches 95% of the $9.66\,MA$ flat-top in $42\,s$, consistent with the register's CD-limited $\sim 43\,s$ ramp (BR-CX-07). The mean ramp rate is $\dot{I}_p \simeq 0.22\,MA/s$ and the inductive loop voltage $V_\ell = L_p \dot{I}_p$ stays below $1.4\,V$ throughout, a factor of several below the level at which vertical or tearing transients are provoked — the quantitative meaning of “disruption-free ramp access.” The driven and bootstrap currents build together toward the exact balance $8.16 + 1.50 = 9.66\,MA$; at flat-top the surface loop voltage falls to zero as the state becomes fully non-inductive and hands off to the current-drive companion [27].

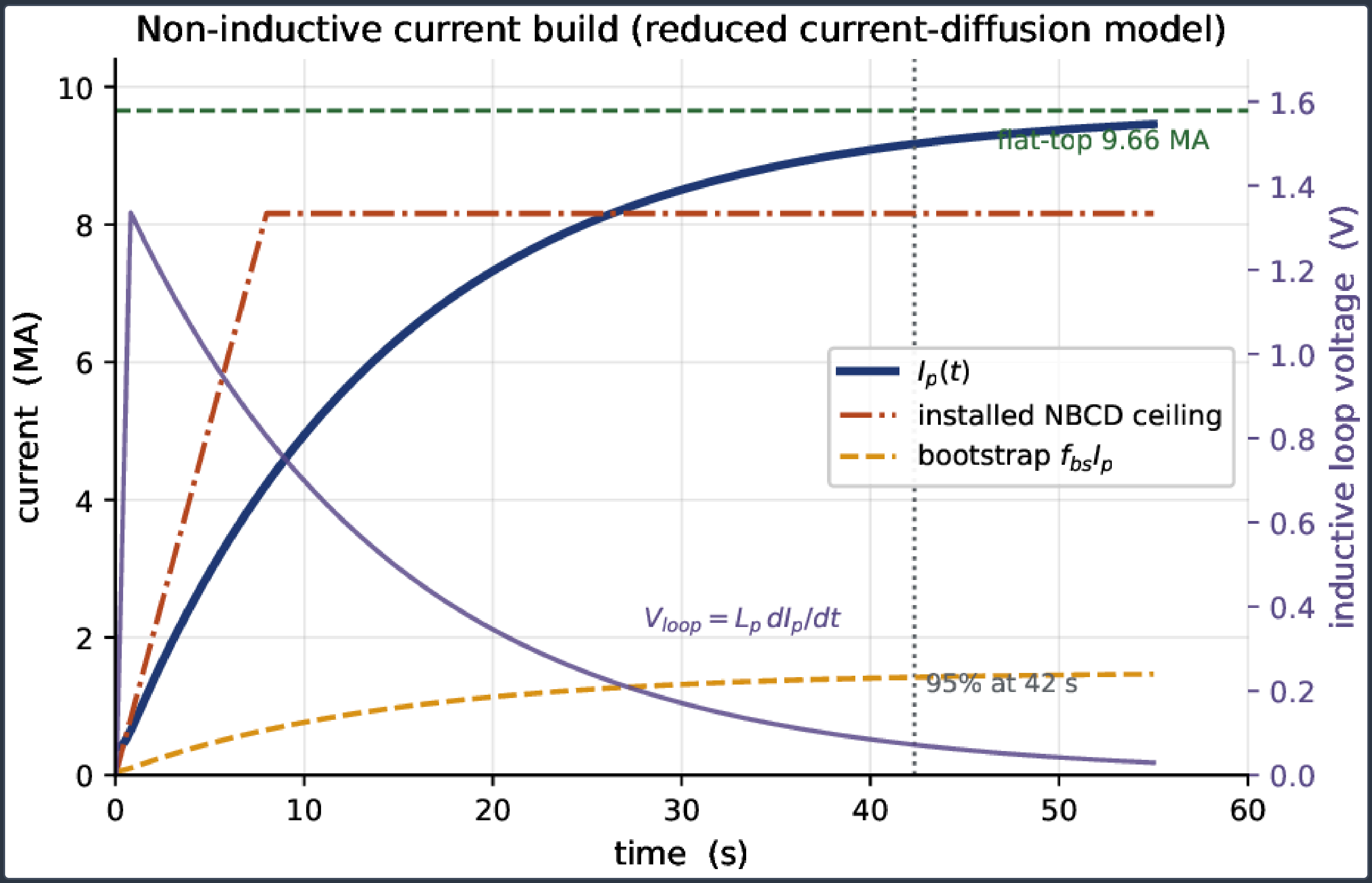

Non-inductive current build from the reduced current-diffusion model (14). $I_p(t)$ reaches 95% of the $9.66\,MA$ flat-top in $42\,s$ at $\dot{I}_p \simeq 0.22\,MA/s$; the inductive loop voltage $V_\ell = L_p \dot{I}_p$ (right axis) stays $< 1.4\,V$. The driven-current ceiling ($8.16\,MA$) and the bootstrap current ($f_{\text{bs}} I_p$) close the balance.

CURRENT-PROFILE EVOLUTION

Figure 4 shows the safety-factor profile at four points along the ramp, reconstructed from a parametrized current-density profile with an off-axis seed component that decays as the beam drive centralises. Early in the ramp the profile is hollow (reversed shear), a natural consequence of off-axis helicity and beam seed deposition, with $q_0 > 1$ so that the axis avoids the $q = 1$ sawtooth boundary. As the current builds and the drive profile broadens, q relaxes to the monotonic flat-top profile with $q_0 \simeq 1.1$ and $q_{95} = 3.0$. Throughout the ramp q_{95} decreases monotonically from above toward 3.0 and never approaches the $q = 2$ external-kink boundary, consistent with the free-boundary equilibrium and ideal-MHD margins reported in the companion paper [28]. Vertical stability at $\kappa = 2.0$ during the ramp is the province of the companion vertical-stability study [29], whose control-coil authority the PF set of [30] provides.

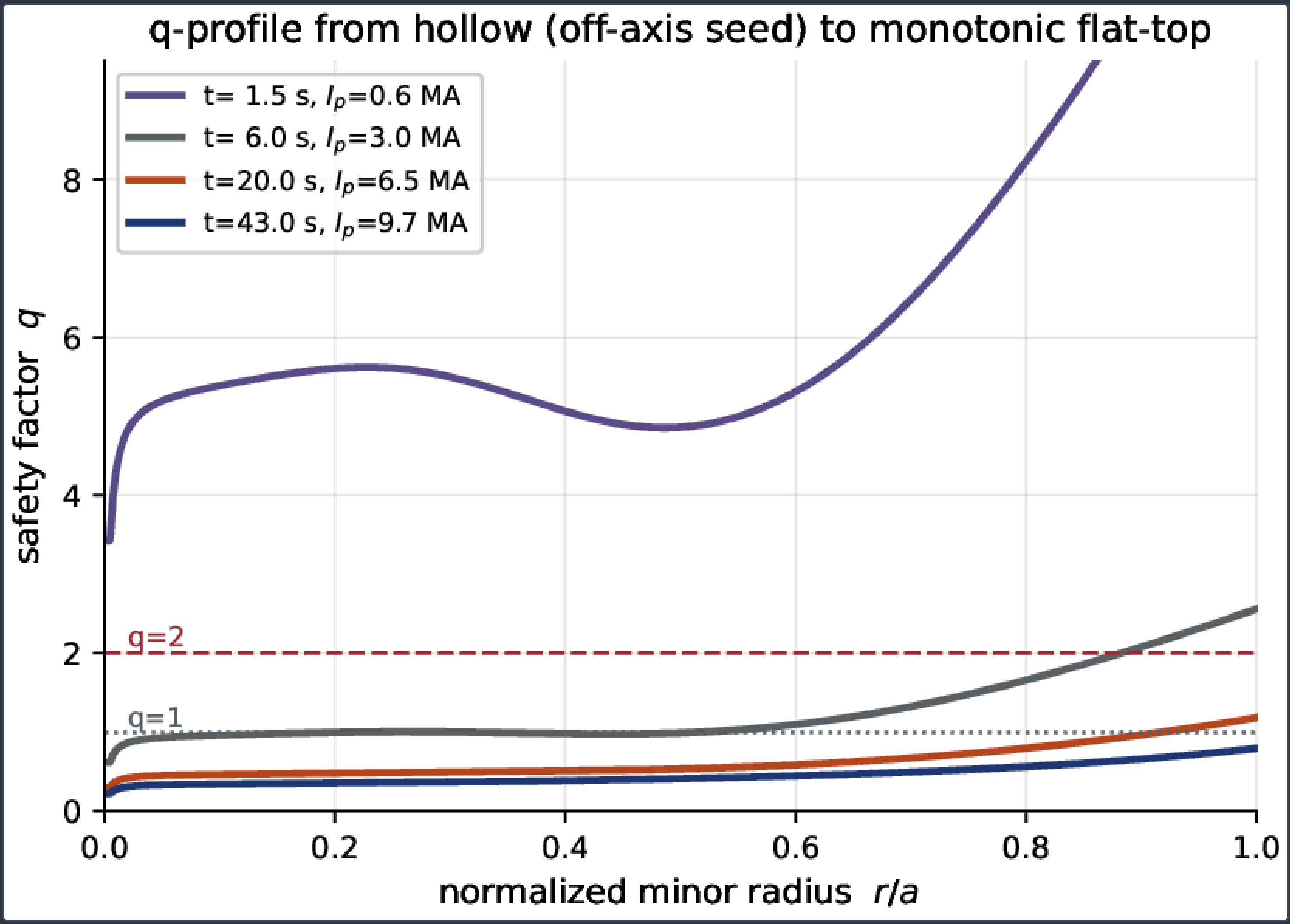

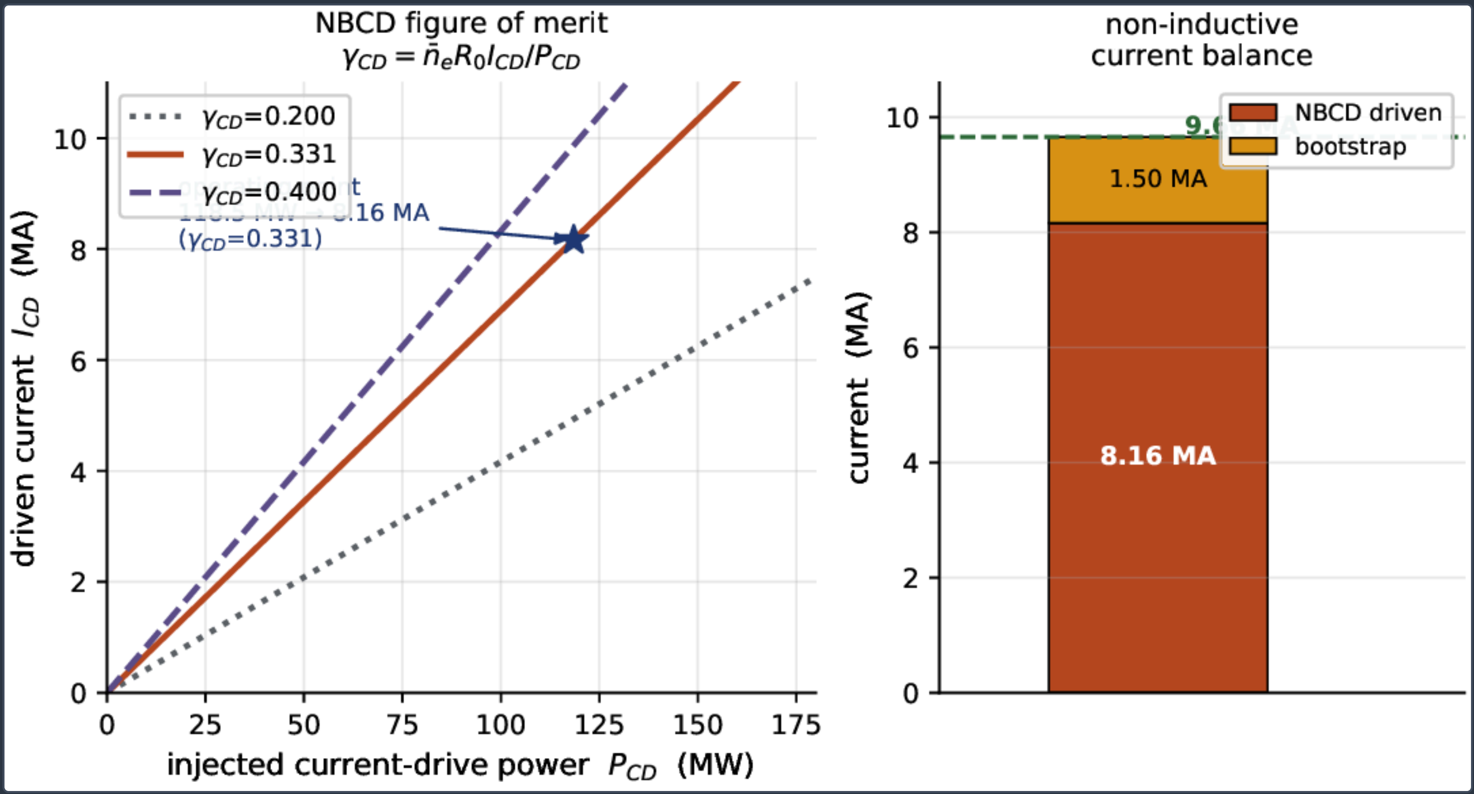

q-profile evolution during the ramp, from a hollow off-axis-seed profile ($t \approx 1.5$ s) to the monotonic flat-top profile ($q_0 \simeq 1.1$, $q_{95} = 3.0$). The axis stays above $q = 1$ and the edge above $q = 2$ throughout.

CURRENT-DRIVE RECONCILIATION

Figure 4 makes the closure of equation (10) explicit. The left panel plots the driven current against installed power for a family of figure-of-merit values spanning the 0.20–0.40 ST band; the Hyperion operating point ($118.5\,MW$, $8.16\,MA$) sits on the $\gamma_{\mathrm{CD}} = 0.331$ curve, reproducing register serial BOM-07. The right panel stacks the driven and bootstrap currents to the $9.66\,MA$ total, showing that the machine is current-drive-dominated (85% driven) with a modest bootstrap contribution. The associated wall-plug demand — eight $1\,MeV$ negative-ion beamlines at a system efficiency that makes the total heating draw several times the fusion power — is the honest cost of a subcritical, current-drive-dominated breeder; it is booked in the heating-and-current-drive actuator companion [33] and carries no economics here.

PRE-IONIZATION ACCESS

Figure 5 evaluates the wave-access condition of §3.3. The ratio ω_{pe}/ω_{ce} is 0.80 in the core — underdense, so the O-mode at the 224 Hertz
$fundamentalisabsorbedandprovidescleanelectron-cyclotronpre-ionizationandheating---andrisesthroughunitytowardtheedge, wheretheplasmaisoverdenseandtheelectronBernsteinwave, reachedbyO--X--Bconversion, istheaccessiblebranch$ laqua2007$.ThisisthephysicalbasisfortheBOM-08sizingof$
\!15$gyrotronsat$1 MW
$: theO-modedoesthecorepre-ionizationandburn-throughofequation$ (???)$, andtheEBWextendsheatingandnon-inductiveassistintotheoverdenseedge.The$
224 tube is at the frontier of gyrotron technology and is flagged as such in the register; it is not a solved procurement.

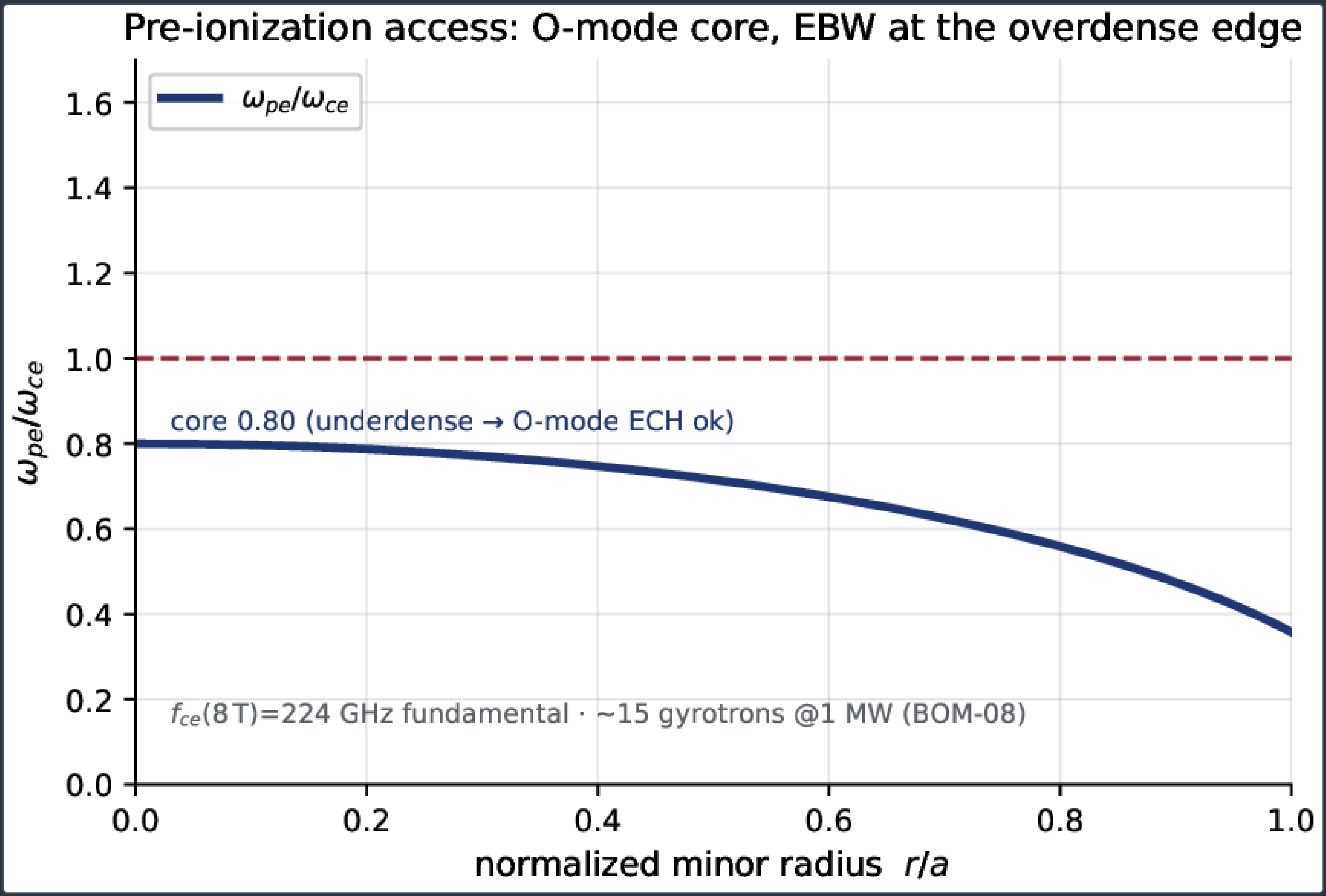

Pre-ionization access. ω_{pe}/ω_{ce} is 0.80 (underdense, O-mode) in the core and exceeds unity (overdense, EBW via O–X–B conversion) toward the edge, at $f_{ce}(8\,T) = 224$ Hertz$ (register BOM-08).

RUNAWAY ENVELOPE AND PRECURSOR MARGINS

The most consequential ramp hazard is a runaway-electron avalanche in the low-density breakdown and early-ramp phase. Figure 6(a) shows the avalanche growing an initial Dreicer seed toward the register plateau band of 4.8–8.2 MA (BR-SX-10) if unmitigated, and the arrest of that growth when the shattered-pellet- injection (SPI) system fires. The design case for *always-armed* SPI rests on a timing margin, quantified in figure 6(b): the SPI physics requires a warning lead of 30 ms, and the precursor stack must clear it. The graph-neural-network state reconstructor gives 8.5 ms of warning on the fastest paths — *below* the SPI requirement — so it cannot be the sole trigger; the physics-informed ramp-to-limit precursor (register BR-CX-31) gives 31 ms and the fused strain-rate/magnetization magnet precursor gives 47.2 ms, both clearing 30 ms. The design conclusion is that the mitigation system must be always-armed and driven by the longer-lead precursors, with the fast GNN warning used as a corroborating rather than a sole trigger — the quantitative content of the "design case for shattered-pellet mitigation" developed in the disruptions companion [31].

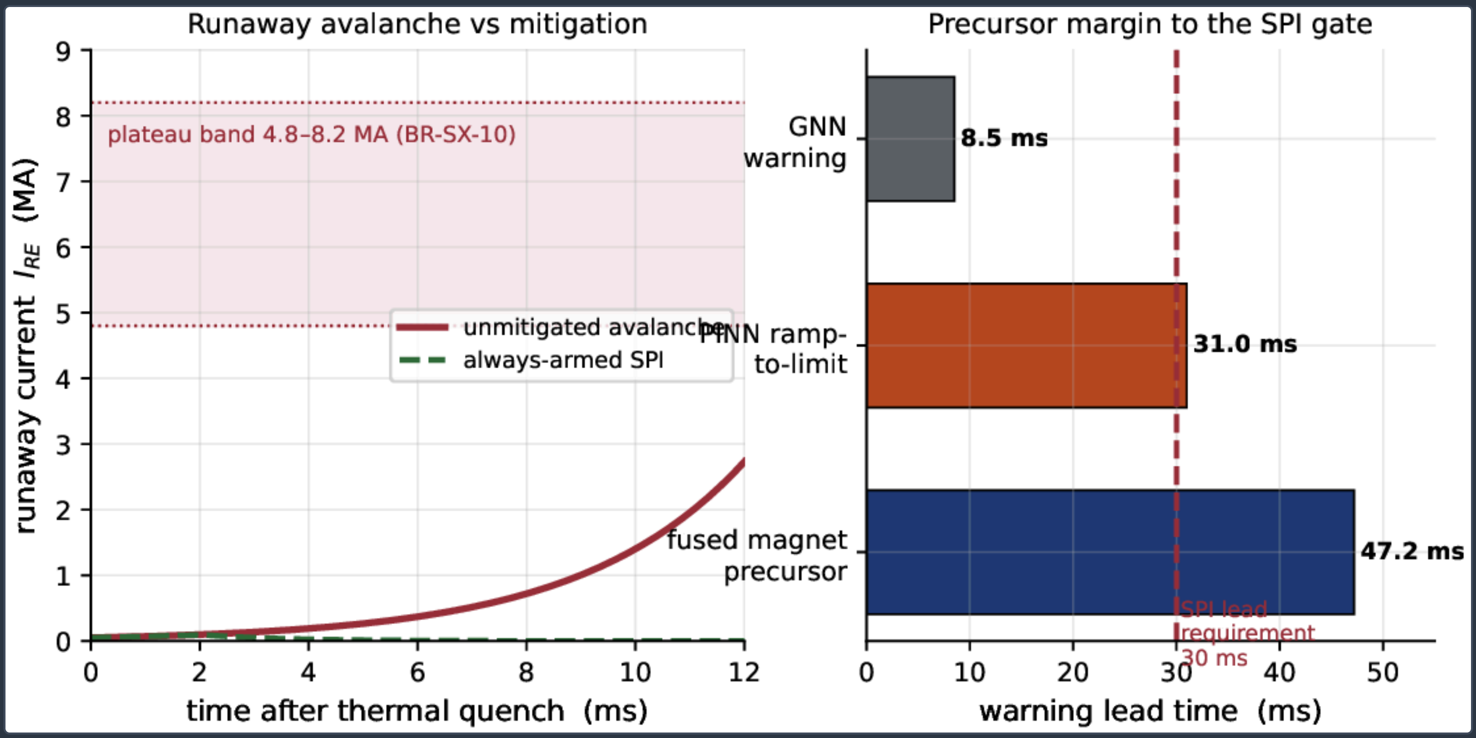

(a) Runaway-electron avalanche toward the 4.8–8.2 MA plateau band (register BR-SX-10) and its arrest by always-armed SPI. (b) Precursor lead times against the 30 ms SPI requirement: the 31 ms physics-informed and 47.2 ms fused-magnet precursors clear it; the 8.5 ms GNN warning does not, so it is corroborating rather than sole.

THE STARTUP SEQUENCE AS A PHASE TABLE

Table 2 collects the four phases with their actuator, the governing relation, and the quantitative target, and figure 7 shows the outboard-PF flux linkage on the negative-triangularity equilibrium that the ramp holds. Together with the flux and current budget of table 1, they constitute the quantified strategy this paper claims: a bounded volt-second demand, a bounded current-drive power, and a limit-avoiding trajectory, each traceable to a frozen register anchor.

PHASE	ACTUATOR	GOVERNS	RELATION	TARGET
I breakdown	ECH/EBW (224 GHz)	burn-through	eq. (9)	~15 MW, O/EBW (BOM-08)
II seed	helicity + beam	seed current	eqs. (7)–(8)	0.1–0.5 MA
III ramp	outboard PF + NBCD	flux + current	eqs. (5),(14)	9.66 MA in ~43 s
IV flat-top	NBCD + bootstrap	sustainment	eqs. (10),(11)	8.16+1.50 MA (hand-off)

The solenoid-free startup sequence. Each phase names its actuator, governing relation, and quantitative target; serials refer to the register [35].

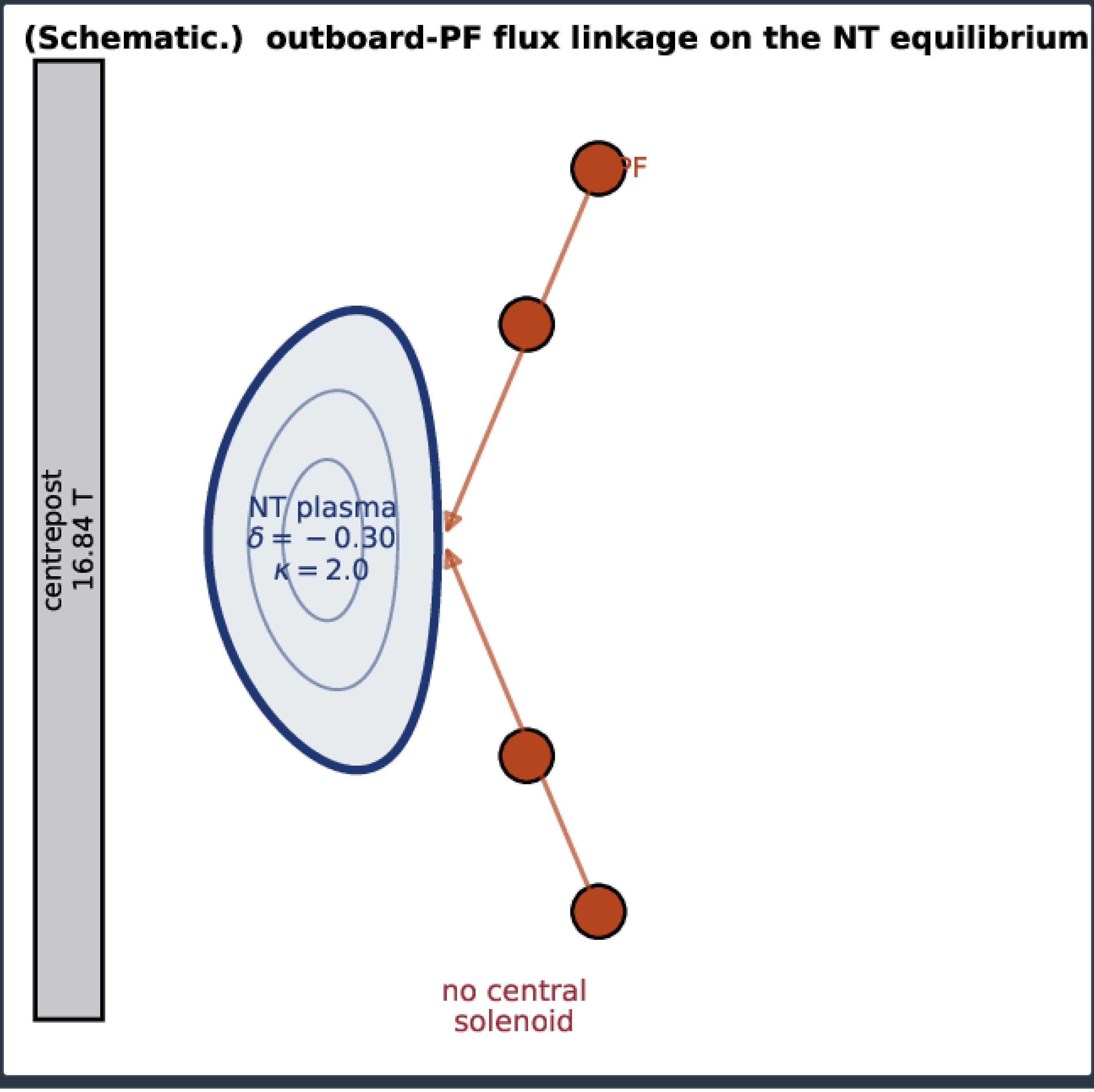
(Schematic.) outboard-PF flux linkage on the NT equilibrium
PF
centrepost
16.84 T
NT plasma
δ = − 0.30
κ = 2.0
no central
solenoid

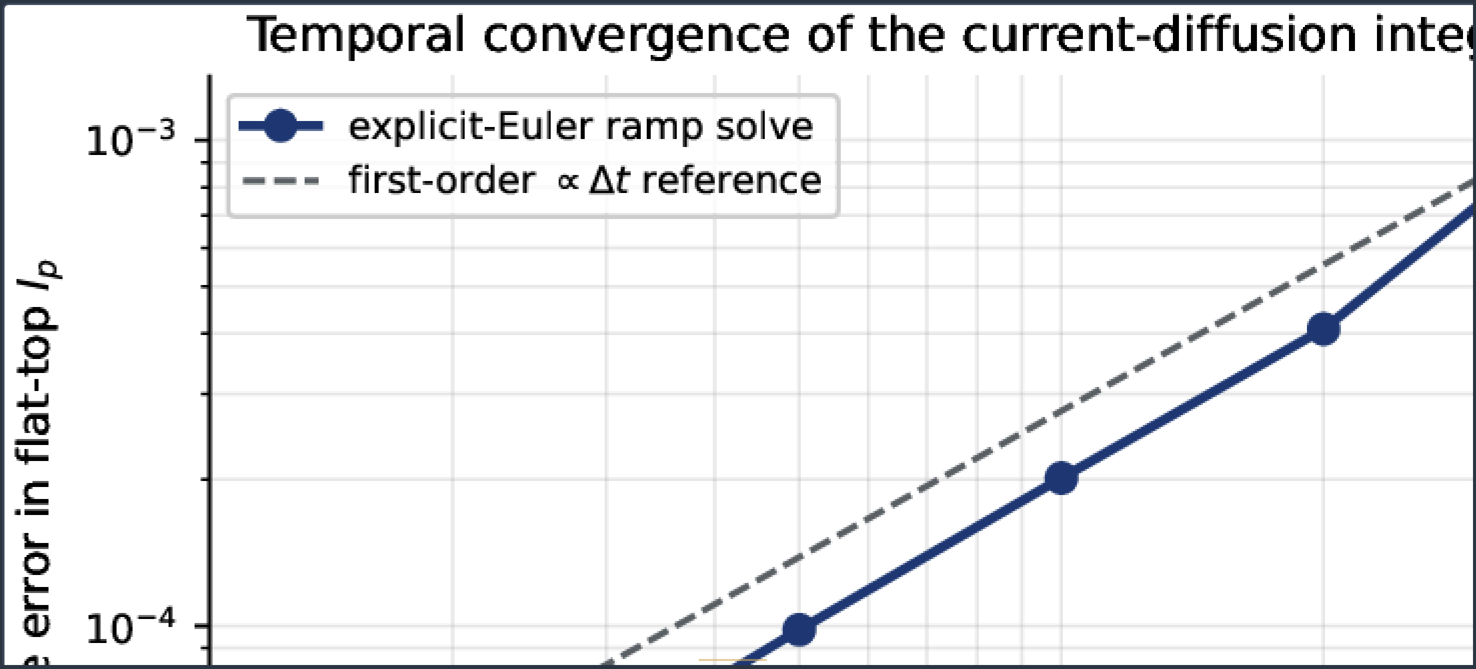
Temporal convergence of the current-diffusion inte
explicit-Euler ramp solve
first-order ∝ Δt reference
10⁻³
10⁻⁴
e error in flat-top I_p

§ 6

Discussion

THE FLUX BUDGET AGAINST THE TOKAMAK-STARTUP RECORD

The inductive flux demand of $\sim 20\,weber$ for a $9.66\,MA$ current is exactly what the half-century-old Ejima scaling predicts: $2.0\,weber/MA$ established on Doublet III near-circular plasmas [14] gives $19.3\,weber$, within 5% of the Hyperion budget and of the register anchor. This is reassuring precisely because it is unsurprising — the volt-second cost of a current channel is set by geometry and resistivity, not by how the flux is delivered, so a solenoid-free machine faces the same $\sim 20\,weber$ that a transformer would have to supply. The novelty is not a smaller number but a different *source*: outboard induction plus the flux linked to the driven current, with the resistive $\sim 6\,weber$ carried continuously by the beams rather than burned from a finite transformer swing.

THE STARTUP TECHNIQUES AGAINST THE ST RECORD

Each ingredient has an experimental precedent that the Hyperion budget stays within. ECH-assisted breakdown at $E \simeq 0.15\,V/m$ on DIII-D [7] establishes that electron-cyclotron pre-ionization removes the need for the large loop voltage an ST cannot supply; the O-mode-core/EBW-edge access of figure 5 is the standard ST picture [8,6]. Transient CHI on NSTX reaching $1\,MA$ from $258\,mweber$ of injector flux [10] establishes that helicity injection can seed a closed-flux current at the $\mathcal{O}(0.1\,MA)$ level Hyperion books for phase II. And bootstrap-aligned non-inductive drive is the operating principle of advanced-tokamak and ST steady-state scenarios generally [13,25]; the Hyperion novelty is only that the bootstrap fraction is *low* (0.155), so the machine leans on current drive rather than on a delicate high-bootstrap alignment. The $\gamma_{CD} = 0.331$ figure of merit is mid-band for a $1\,MeV$ negative-ion beam at these parameters [11]. Where the compact ST record is thinnest — a controlled, closed-loop ramp to near-$10\,MA$ on a reactor-scale machine — is where we are most careful to claim a quantified strategy rather than a demonstrated sequence (§7). Modern high-field STs such as ST40 [26] and the NSTX-U class [25] are the machines on which the individual ingredients are being pushed toward the reactor regime.

RELATION TO THE RAMP CONTROLLER

The trajectory here is open-loop: it shows that a bounded flux and power budget *admits* a limit-avoiding path to flat-top. Closing the loop — rejecting disturbances, holding q and density inside the corridor, and detecting the ramp-to-limit precursor in real time — is the task of the solenoid-free ramp controller in the breeder control-suite companion [32], whose acceptance test is precisely "reaches $9.66\,MA$ flat-top in simulation without a solenoid" (register KFE-CF-BR-004). The present paper supplies that controller its reference trajectory and its safety corridor; the controller supplies the closed-loop guarantee this paper does not claim.

§ 7

Limitations

Two honest gates bound the claims. *First, the ramp is a quantified strategy, not a demonstrated controlled sequence.* The flux budget, the current-drive closure, the density and q corridors, and the precursor margins are each computed and each traces to a frozen anchor, but the ramp has not been closed in a self-consistent, disturbance- rejecting, closed-loop simulation of the full plant; that is the deliverable of the ramp controller [32], and until it is met the ramp is booked as a carried engineering risk. *Second, the bootstrap fraction carries a model-to-model spread that we report rather than average away*. The Sauter formulation gives $f_{bs} = 0.155$ at the frozen operating point (register BR-L2-A6), while an independent NEO drift-kinetic integration and a `cfspopcon` 0-D scaling place it lower, near $0.056–0.075$, at flat density and reduced-order geometry (register flag BR-L2-A16). The direction is consistent — all three agree the machine is current-drive-dominated — and the difference is favourable to the startup case, since a lower bootstrap fraction means the ramp depends even more on the well-characterised beam drive and less on a self-consistent high-bootstrap alignment. But the spread is real, we do not collapse it to a single point, and a full-profile bootstrap reconciliation is a named open work item. Neither gate changes the paper's claim, which is a bounded, limit-avoiding budget, not a solved sequence.

§ 8

Conclusion

A spherical tokamak has no room for a central solenoid, so the Hyperion breeder must be born and grown without a transformer. We have written the governing equations of that start — the poloidal-flux diffusion equation with a non-inductive source (4), the Poynting/Ejima volt-second balance (1), the helicity-injection balance (7), the electron-cyclotron burn-through balance (9), and the current-drive figure of merit (10) — and closed the budget against the frozen anchors. The inductive flux demand of $20.3\,weber$ resolves the register's $20\,weber$ and matches the empirical Ejima rule to 5%; a reduced current-diffusion integrator whose non-inductive fixed point is $I_{\mathrm{CD}}/(1-f_{\mathrm{bs}}) = 8.16/0.845 = 9.66\,MA$ reaches 95% of flat-top in $42\,s$ at $0.22\,MA/s$ and a loop voltage below $1.4\,V$; the driven ($8.16\,MA$, $118.5\,MW$, $\gamma_{\mathrm{CD}} = 0.331$) and bootstrap ($1.50\,MA$) currents close the balance exactly; the ramp stays a factor 3.3 below the Greenwald limit and above $q = 2$ throughout; and a runaway-electron plateau of 4.8–$8.2\,MA$ is met by a precursor stack clearing the $30\,ms$ SPI requirement. The machine starts and ramps its current without a central solenoid, using electron-cyclotron pre-ionization, a helicity or beam seed, and neutral-beam current drive, then hands off to the non-inductive and bootstrap currents that hold the $9.66\,MA$ flat-top. The remaining risk is the closed-loop ramp control and the bootstrap-fraction reconciliation, both flagged and both booked to named companions.

Acknowledgments tocsectionAcknowledgments Part of the Kronos Fusion Energy 2026 design series. The authors thank the Kronos physics de-risking programme for the frozen result set underlying every quantitative claim, and the computational team for the NVIDIA GPU HPC campaign.

Reproducibility. Every headline quantity in this paper is a frozen anchor in the Kronos Physics De-Risking Register [35] (doi:10.5281/zenodo.22133057): the flux-budget partition and ramp trajectory (BR-CX-07), the neutral-beam current-drive architecture (BOM-07), the bootstrap fraction (BR-L2-A6/A16), the ECH/EBW access (BOM-08), the runaway plateau (BR-SX-10) and the ramp-to-limit precursor (BR-CX-31). Each figure is regenerable from the deposited generation script and the register anchors; this paper is archived at doi:10.5281/zenodo.22645760; official version: https://www.kronosfusionenergy.com/publications/solenoid-free-startup.html. No result depends on unpublished or proprietary data, and no economic analysis is part of the public deposit.

Data availability tocsectionData availability The flux budget, ramp trajectory, q-profile, current-drive, wave-access and runaway-precursor data used for figures 2–7 are archived with the deposit at doi:10.5281/zenodo.22645760 and trace to the register [35] by the serial identifiers cited inline. No economics appear in the public deposit.

Competing interests tocsectionCompeting interests Provisional patent applications relating to aspects of this work have been filed.

tocsectionReferences

APPARATUS

Portfolio, People & Record

The intellectual-property estate, the people who built it, the limitations that gate it, and the sources it rests on.

1	4	40	27
GRANTED PATENT	2026 PROVISIONALS	TEAM MEMBERS	2022 PROVISIONALS

INTELLECTUAL PROPERTY

The patent portfolio

The estate spans a granted high-field magnet patent, pending utility and 2026 provisional filings that map to the two products, a digital-twin control provisional, a registered trademark application, and the original 2022 provisional family. Every patentable disclosure in the five-paper arXiv drop was protected **before** publication: the breeder and burner provisionals were filed 1–2 August, and a publication-gap omnibus filing the evening before the drop swept up the DEC, plasma-control, and REBCO-winding matter of the three otherwise-unprotected papers. Patent numbers and application serials are matters of public record; claim scope is summarised, not reproduced.

GRANTED & PENDING UTILITY

US 12,009,112	High-field tilted graded-REBCO magnet architecture (KRONO-002A) · *app. 17/878,550*	GRANTED
US 17/878,507	Core device / method (KRONO-001A) · *utility*	PENDING

2026 PROVISIONAL FILINGS — MAPPED TO THE PRODUCTS

64/124,209	Hyperion — spherical-tokamak tritium / helium-3 foundry · *breeder · filed Aug 2026*	FILED
64/124,220	Aegis / MetroVolt — synchrotron-cutoff, fuel-selection & plug-winding · *generator · filed Aug 2026*	FILED
64/115,167	KRONOS-CTRL digital-twin plant control · *provisional · filed Jul 2026*	FILED
64/005,440	Integrated spherical-tokamak fusion architecture · *early integrated-architecture filing · filed Mar 2026*	FILED
64/105,530	Negative-triangularity spherical-tokamak architecture · *foundational ST filing · filed Jul 2026*	FILED
64/128,097	Publication-gap omnibus — quasineutral two-species expander DEC · provenance-gated / latency-split plasma control · as-built high-field winding & conductor architecture · *filed 7 Aug 2026, the evening before the arXiv drop*	FILED

TRADEMARK & ORIGIN

FTK-98801894	Kronos Fusion Energy — trademark application	FILED
KR-2022-*	Original provisional family (KR-2022-00001 … 00027) · *27 filings, 2022*	PRIORITY

The narrow, defensible magnet novelty — the specific conductor and the digital-twin winding optimisation, not high-field REBCO as a category — is the commercial core that can earn ahead of any Q > 1 milestone, with markets in fusion magnet supply, MRI/NMR, accelerators, and proton therapy. The claim is scoped honestly: the high field is a *system field* result, not a stand-alone-coil record; the small-bore plug coil is structurally infeasible as a bare winding but resolved by a stress-managed structural shield (feasible-pending-FEA); and the winding-tape experiment returned a *null result*. The value is the method, not a field record.

THE TEAM

Founding partners, board, advisors & auditors

Kronos is built by a bench of advanced-fuel-fusion, high-field-magnet, direct-conversion, and materials specialists, with a board and operations team drawn from defense, national laboratories, and industry. Dates are shown as ranges; where a tenure has ended or is term-ending, the range says so.

FOUNDING PARTNERS — SCIENCE

Dr. Gerald Kulcinski
Co-Founder · Helium-3 & Advanced-Fuel Fusion
UW–Madison · 2023–Present

Dr. Carl Weggel
Chief Scientist / S.M.A.R.T. Design
MIT Alcator Program · 2022–Present

Dr. Robert J. Weggel
Magnetic Field Design
MIT Magnet Lab · 2022–Present

BOARD

Priyanca Ford
Founder & CEO · Executive Board
2022–Present

Bandel Carano
Finance / Strategy
Oak Investment Partners / Stanford · 2025–2026

Patrick Schweiger
Fusion Device Engineering
Oklo / CFS / TerraPower · 2025–Present

SCIENTIFIC ADVISORS

Dr. Steven O. Dean
Fusion Policy & History
DOE / Fusion Power Associates · 2025–Present

Dr. Patrick H. Diamond
Plasma Turbulence & Transport
UC San Diego · 2025–Present

Dr. Jack J. Dongarra
HPC & Numerical Algorithms
Turing Award · 2025–Present

Dr. Nasr M. Ghoniem
Chief Material Scientist
UCLA · 2025–Present

Dr. Siegfried Glenzer
Plasma Physics & Laser Fusion
Stanford / SLAC · 2022–Present

Dr. David A. Hammer
Pulsed-Power Fusion
Cornell · 2025–Present

Dr. Donald A. Spong
Plasma Theory & Confinement
ORNL · 2025–Present

Dr. Curtis Smith
Risk Assessment & Nuclear PRA
MIT / Idaho National Lab · 2025–Present

RADM (Ret.) David Goggins
Naval Engineering & Power-Plant Design
U.S. Navy · 2023–2026

Dr. Konstantin Batygin
Mathematician
Caltech · 2022–2025

Dr. Ruben Fair
Magnet Design / ITER Liaison
PPPL / Jefferson Lab · 2022–2025

Dr. Paul S. Weiss
Materials & Nanotechnology
UCLA · 2022–2025

SCIENTIFIC AUDITORS

Dr. Wilfred A. Cooper
Plasma Equilibrium Theory
EPFL / Swiss Plasma Center · 2025–Present

Dr. Ahmed Hassanein
Plasma–Material Interactions
Purdue / Argonne · 2025–Present

Dr. Patrick E. Hopkins
Extreme Thermal Materials
U. of Virginia · 2025–Present

Dr. Peter Hosemann
Materials Joining & Structural Integrity
UC Berkeley · 2025–Present

Dr. Travis W. Knight
Advanced Nuclear Fuels & Systems
U. of South Carolina · 2025–Present

Dr. Philippe Lebrun
Cryogenics & Magnet Cooling
CERN · 2025–Present

Dr. Nitendra Singh
Nuclear Safety & Fuel Cycle
ITER · 2025–Present

Dr. Guido Van Oost
Magnetic Confinement & Fusion Systems
Ghent University · 2025–Present

Dr. Gary S. Was
Radiation Materials & Structural Integrity
U. of Michigan · 2025–Present

Dr. Ray Sedwick
Direct Energy Conversion
U. of Maryland · 2025

OPERATIONS

Michael Laughlin
Chief Operating Officer
2022–Present

Martin Owens
Chief Strategy Officer
LANL / GE Hitachi · 2022–Present

MG (Ret.) Paul Pardew
Chief Contracting Officer
Army Contracting Command · 2022–Present

David Beck
Fusion Commercialization
U.S. Space Force · 2024–Present

Sushma Bhatia
Environmental & Legislative
Google · 2022–Present

Michael De Frenza
Technology Licensing
2023–Present

MG (Ret.) Robin L. Fontes
Cybersecurity & Defense
Army Cyber Command · 2022–Present

Vijay Gehani
Supply Chain & Components
INOX India · 2024–Present

Jon Michel Greenwood
IT & AI Infrastructure
Live Nation · 2023–Present

Brian C. O'Neill
National Security
CIA / ODNI · 2022–Present

Gen. (Ret.) Gustave F. Perna
DoD Liaison
Operation Warp Speed · 2022–2023

Andrea Romero
Marketing Lead
2022–Present

Legal counsel is retained; those roles are held on the internal roster and are not listed here.

SOURCES

References

1 J E Menard *et al*, Fusion nuclear science facilities and pilot plants based on the spherical tokamak, *Nucl. Fusion* **56** 106023 (2016). doi:10.1088/0029-5515/56/10/106023

2 M Ono *et al*, Exploration of spherical torus physics in the NSTX device, *Nucl. Fusion* **40** 557 (2000). doi:10.1088/0029-5515/40/3Y/316

3 A Sykes *et al*, First results from MAST, *Nucl. Fusion* **41** 1423 (2001). doi:10.1088/0029-5515/41/10/310

4 M E Austin *et al*, Achievement of reactor-relevant performance in negative triangularity shape in the DIII-D tokamak, *Phys. Rev. Lett.* **122** 115001 (2019). doi:10.1103/PhysRevLett.122.115001

5 A Marinoni, O Sauter and S Coda, A brief history of negative triangularity tokamak plasmas, *Rev. Mod. Plasma Phys.* **5** 6 (2021). doi:10.1007/s41614-021-00054-0

6 R Raman and V F Shevchenko, Solenoid-free plasma start-up in spherical tokamaks, *Plasma Phys. Control. Fusion* **56** 103001 (2014). doi:10.1088/0741-3335/56/10/103001

7 B Lloyd, G L Jackson, T S Taylor, E A Lazarus, T C Luce and R Prater, Low voltage Ohmic and electron cyclotron heating assisted startup in DIII-D, *Nucl. Fusion* **31** 2031 (1991). doi:10.1088/0029-5515/31/11/001

8 H P Laqua, Electron Bernstein wave heating and diagnostic, *Plasma Phys. Control. Fusion* **49** R1 (2007). doi:10.1088/0741-3335/49/4/R01

9 V F Shevchenko *et al*, Electron Bernstein wave assisted plasma current start-up in MAST, *Nucl. Fusion* **50** 022004 (2010). doi:10.1088/0029-5515/50/2/022004

10 R Raman *et al*, Demonstration of tokamak ohmic flux saving by transient coaxial helicity injection in the National Spherical Torus Experiment, *Phys. Rev. Lett.* **104** 095003 (2010). doi:10.1103/PhysRevLett.104.095003

11 N J Fisch, Theory of current drive in plasmas, *Rev. Mod. Phys.* **59** 175 (1987). doi:10.1103/RevModPhys.59.175

12 O Sauter, C Angioni and Y R Lin-Liu, Neoclassical conductivity and bootstrap current formulas for general axisymmetric equilibria and arbitrary collisionality regime, *Phys. Plasmas* **6** 2834 (1999). doi:10.1063/1.873240

13 C Gormezano *et al*, Progress in the ITER Physics Basis Chapter 6: Steady state operation, *Nucl. Fusion* **47** S285 (2007). doi:10.1088/0029-5515/47/6/S06

14 S Ejima *et al*, Volt-second analysis and consumption in Doublet III plasmas, *Nucl. Fusion* **22** 1313 (1982). doi:10.1088/0029-5515/22/10/006

15 L Spitzer and R H\"arm, Transport phenomena in a completely ionized gas, *Phys. Rev.* **89** 977 (1953). doi:10.1103/PhysRev.89.977

16 F Felici *et al*, Real-time physics-model-based simulation of the current density profile in tokamak plasmas, *Nucl. Fusion* **51** 083052 (2011). doi:10.1088/0029-5515/51/8/083052

17 S C Jardin, N Pomphrey and J Delucia, Dynamic modeling of transport and positional control of tokamaks, *J. Comput. Phys.* **66** 481 (1986). doi:10.1016/0021-9991(86)90077-X

18 N C Amorisco *et al*, FreeGSNKE: a Python-based dynamic free-boundary toroidal plasma equilibrium solver, *Phys. Plasmas* **31** 042517 (2024). doi:10.1063/5.0188467

19 G M Staebler, J E Kinsey and R E Waltz, A theory-based transport model with comprehensive physics, *Phys. Plasmas* **14** 055909 (2007). doi:10.1063/1.2436852

20 E Hirvijoki *et al*, ASCOT: solving the kinetic equation of minority particle species in tokamak plasmas, *Comput. Phys. Commun.* **185** 1310 (2014). doi:10.1016/j.cpc.2014.01.014

21 M Hoppe, O Embreus and T F\"ul\"op, DREAM: A fluid-kinetic framework for tokamak disruption runaway electron simulations, *Comput. Phys. Commun.* **268** 108098 (2021). doi:10.1016/j.cpc.2021.108098

22 M N Rosenbluth and S V Putvinski, Theory for avalanche of runaway electrons in tokamaks, *Nucl. Fusion* **37** 1355 (1997). doi:10.1088/0029-5515/37/10/I03

23 B N Breizman, P Aleynikov, E M Hollmann and M Lehnen, Physics of runaway electrons in tokamaks, *Nucl. Fusion* **59** 083001 (2019). doi:10.1088/1741-4326/ab1822

24 J Candy, E A Belli and R V Bravenec, A high-accuracy Eulerian gyrokinetic solver for collisional plasmas, *J. Comput. Phys.* **324** 73 (2016). doi:10.1016/j.jcp.2016.07.039

25 J E Menard *et al*, Overview of the physics and engineering design of NSTX upgrade, *Nucl. Fusion* **52** 083015 (2012). doi:10.1088/0029-5515/52/8/083015

26 S A M McNamara *et al*, Achievement of ion temperatures in excess of 100 million degrees Kelvin in the compact high-field spherical tokamak ST40, *Nucl. Fusion* **63** 054002 (2023). doi:10.1088/1741-4326/acbec8

27 P I Ford and G L Kulcinski, Bootstrap-aligned steady-state current sustainment without a central solenoid: NBCD, ECCD and LHCD for a compact spherical-tokamak breeder, Kronos Fusion Energy 2026 series. doi:10.5281/zenodo.22645758

28 P I Ford and G L Kulcinski, Free-boundary equilibrium and ideal-MHD stability of a compact spherical-tokamak breeder, Kronos Fusion Energy 2026 series. doi:10.5281/zenodo.22645740

29 P I Ford, Vertical stability at high elongation: displacement growth rates, control-coil authority and VDE avoidance for a compact spherical-tokamak breeder, Kronos Fusion Energy 2026 series. doi:10.5281/zenodo.22645834

30 P I Ford, R J Weggel and C Weggel, Poloidal-field coil set and equilibrium-current optimization for a compact spherical-tokamak breeder, Kronos Fusion Energy 2026 series. doi:10.5281/zenodo.22645945

31 P I Ford and G L Kulcinski, Disruptions, runaway-electron avalanche and electromagnetic loads in a compact spherical-tokamak breeder: the design case for shattered-pellet mitigation, Kronos Fusion Energy 2026 series. doi:10.5281/zenodo.22645724

32 P I Ford, A real-time control suite for a compact negative-triangularity spherical-tokamak breeder: profile, shape, vertical-stability, q-profile and solenoid-free ramp controllers, Kronos Fusion Energy 2026 series. doi:10.5281/zenodo.22645809

33 P I Ford and G L Kulcinski, Heating and current-drive actuator systems for a compact spherical-tokamak breeder: an NBI/ECH/ICRF/LHCD mix optimized for solenoid-free sustainment, Kronos Fusion Energy 2026 series. doi:10.5281/zenodo.22645872

34 P I Ford and G L Kulcinski, Negative-triangularity turbulence suppression in a compact spherical-tokamak breeder: nonlinear gyrokinetics of ion- and electron-scale quiescence at the operating point, Kronos Fusion Energy 2026 series. doi:10.5281/zenodo.22645722

35 P I Ford, *Kronos Physics De-Risking Register*, v8, Kronos Fusion Energy 2026 series. doi:10.5281/zenodo.22133057

COLOPHON

How this document was made

The Kronos Fleet — Combined Editorial, 2026 is set in **Fraunces** (display), **Gelasio** (text), and **IBM Plex Mono** (data & equations), carried forward from the Kronos editorial design system.

The figures are rendered at 300 dpi from the deposited generator scripts; the document is composed as a single self-contained file with embedded fonts and imagery, paginated to US Letter, and rendered to PDF through a headless Chromium engine in matched light and dark editions.

Every headline quantity carries an evidence class; withdrawn and restated values are marked as such. Nothing herein is frozen beyond the founder-approved Tier-A set.

Explore it live — turn the interactive 3-D model, run the deposited solvers in the physics validator, and watch the companion film series.

LEGAL NOTICE

Notice, status, and distribution

Conceptual design & simulation study. This document reports a conceptual design and simulation study. It is not a construction commitment, a safety-analysis report, a regulatory filing, or an offer of securities. Forward-looking statements — schedules, costs, market sizes, and performance — are estimates subject to the limitations set out in the Simulations part and may change.

Numbers and their classes. Quantities are reported with evidence classes and case labels; modelled, assumed, and requirement-class values are identified as such and are not to be quoted without their labels.

Public edition. This edition carries the physics and design only; all financial, funding, and defense-commercial content has been removed for public distribution. The scientific text corresponds to the arXiv and journal submissions.

THE 2026 KRONOS SERIES

One programme, many papers

This editorial is one paper in the Kronos 2026 series — a real fusion company's complete, reproducible physics record for a spherical-tokamak breeder and its low-neutron D–^{3}He tandem-mirror burners. Every headline number is a frozen anchor in the Physics De-Risking Register.

Explore the whole programme: the De-Risking Register, the interactive 3-D model, and the physics validator.

KRONOS FUSION ENERGY

From Breakdown to Flat-Top: Solenoid-Free Startup and Disruption-Free Ramp Access for a Negative-Triangularity Spherical-Tokamak Breeder

A real fusion company building real machines. Explore the science, live.

Zenodo · doi:10.5281/zenodo.22645760

Read on kronosfusionenergy.com

The Physics De-Risking Register